Electronic Supplementary information

An all 2D Fe-FET retinomorphic sensor based on novel gate dielectric $In_2Se_{3-x}O_x$

Xuhong Li,[a,b] Xiaoqing Chen,[b] Wenjie Deng,[b] Songyu Li,[a] Boxing An,[c] Feihong Chu,[c] Yi Wu,[c]*

*Famin Liu, *[a] Yongzhe Zhang *[b]*

1. School of Physics, Beihang University, Beijing 100191, China

2. Key Laboratory of Optoelectronics Technology, College of Microelectronics, Faculty of Information Technology, Beijing University of Technology, Beijing 100124, China

3. Faculty of Materials and Manufacturing, Beijing University of Technology, Beijing 100124, China

*Corresponding Authors: chenxiaoqing@bjut.edu.cn, fmliu@buaa.edu.cn and yzzhang@bjut.edu.cn

Supplementary Note 1. Supporting information for the experimental data.

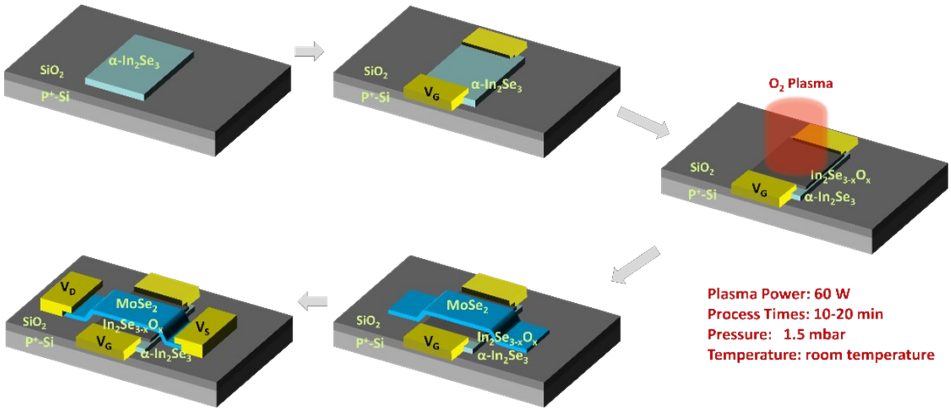

Figure S1. The fabrication processes and the used plasma conditions of the all 2D ferroelectric field effect transistor device. The power of the oxygen plasma treatment is 60 W. The process time range is 10-20 minutes and the pressure is 1.5 mbar. The oxygen plasma process was performed at room temperature.

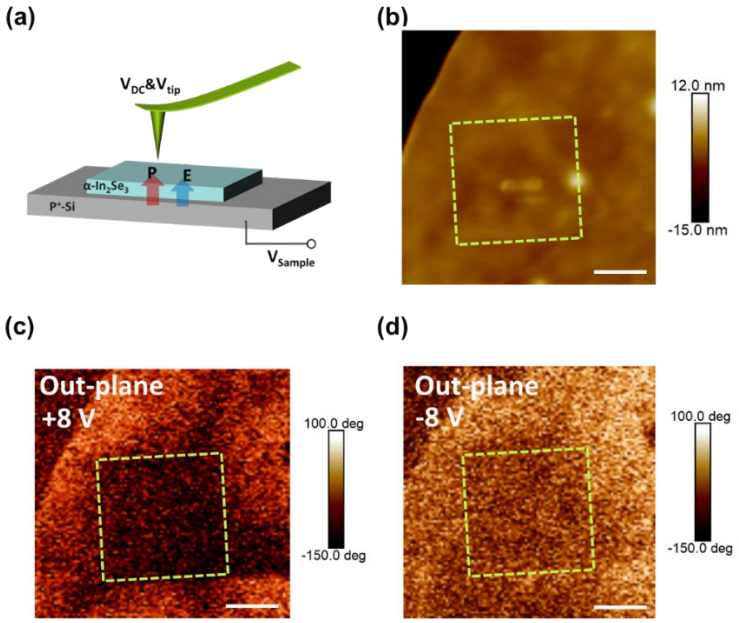

Figure S2. (a) Schematic of the switching of out-of-plane (OOP) polarizations direction with OOP electric field. (b) The AFM topography of a α-In_2Se_3 on p+-Si substrate. The scale bar is 600 nm. (c) The OOP PFM phases after 8 V bias writing in the indicated yellow dash square and (d) The OOP PFM phases after -8 V bias writing in the indicated yellow dash square. The change of OOP PFM phase implies that the OOP electric polarizations can be reversibly flipped by the OOP bias of the α-In_2Se_3 device in (a).

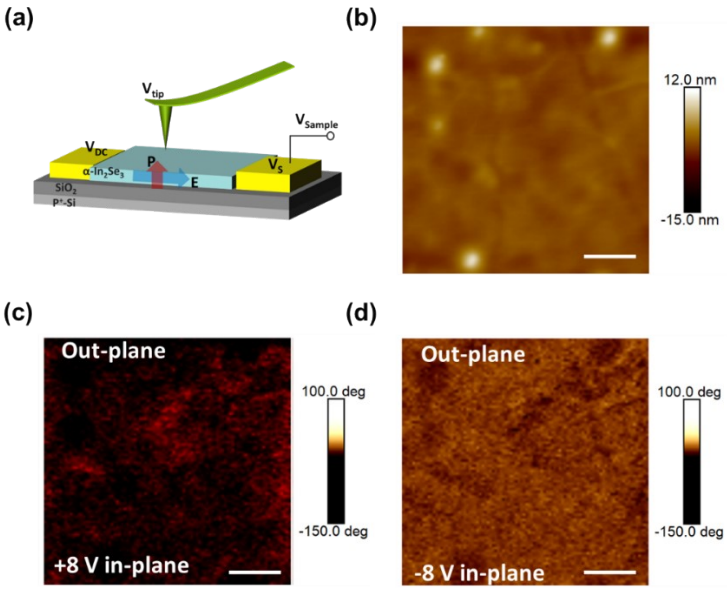

Figure S3. (a) Schematic of the switching of OOP polarizations direction with In-plane (IP) electric field. (b) The AFM topography of a α-In_2Se_3 on SiO_2/p+-Si substrate. The scale bar is 600 nm. (c) The OOP PFM phases after 8 V bias writing in IP electric field and (d) The OOP PFM phases after -8 V bias writing in IP electric field. The OOP electric polarizations also can be reversibly flipped by the IP bias of the proposed device in (a). The strong correlation between OOP and IP polarization direction of the α-In_2Se_3 can be confirm. That is, the polarization direction in one direction can be manipulated through the other direction.[1]

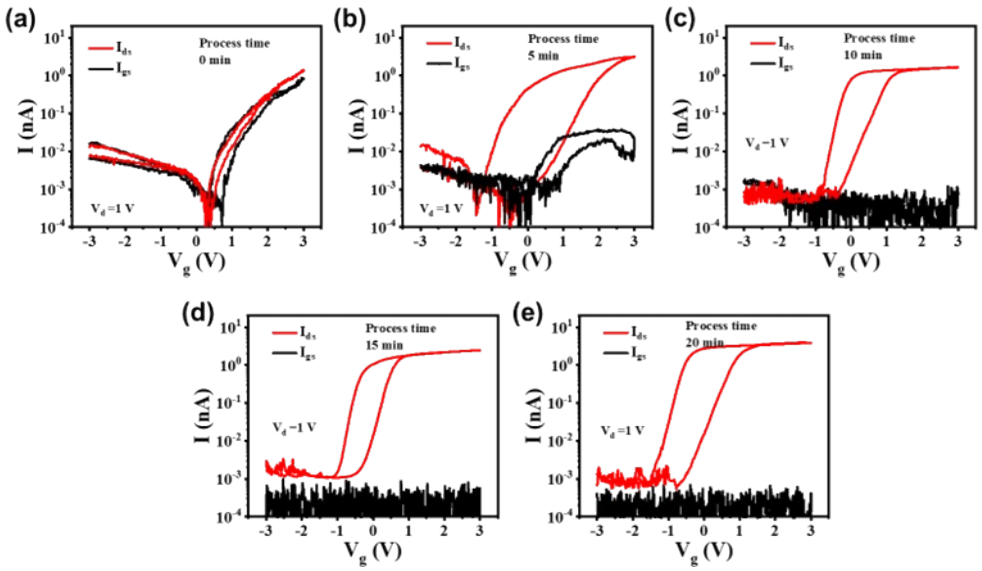

Figure S4. The leakage currents and transfer curves at different oxygen treatment times. With the oxygen treatment time increases, the gate leakage current of the device gradually decreases due to the increase of the oxygen composition in the dielectric layer.[2] When the oxygen treatment time exceeds 10 minutes, this gate leakage currents approach the resolution limit of the test equipment.

(a)

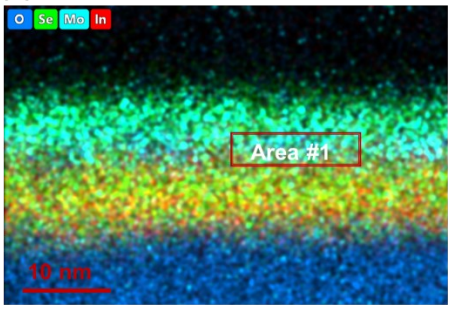

(b)

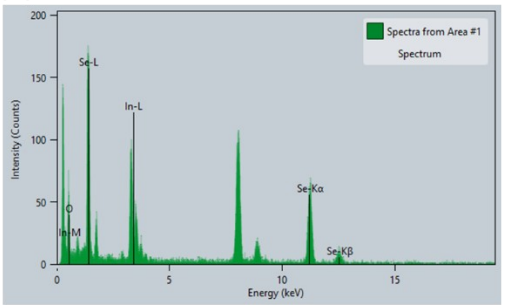

(c)

Element	Z	Family	Net intensity	Net background	K-factor	Atomic fraction	Mass fraction	Fit error
-	-	-	counts	counts	-	%	%	%
O	8	K	681.49	126.64	1.00	27.86	6.25	1.86
Se	34	K	2433.69	260.98	2.22	44.65	49.46	0.56
In	49	L	3422.13	876.81	1.37	27.49	44.29	0.48

Figure S5. The estimated elemental composition of the obtained $In_2Se_{3-x}O_x$ by oxygen plasma treatment. As shown in the red font in Figure 5(c), the ratio of the number of the In elements to the sum of Se and O elements is less than 2:3. The possible reason is that the excess EDS signals from the Se elements in the $MoSe_2$ region are collected. The corresponding modifications have been performed in the Supporting information.

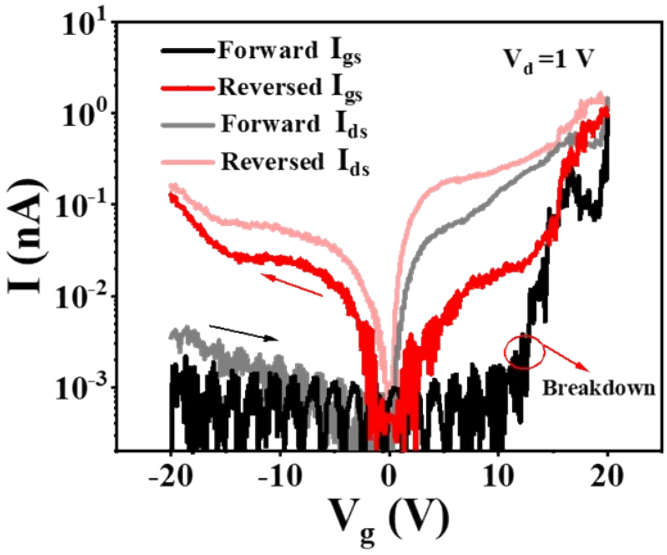

Figure S6. The gate leakage current and the transfer curve of this ferroelectric transistor on a wider gate bias range (-20 V-20 V). When the gate voltage exceeds 10 V, the unwanted large gate leakage current is found as shown by the black line of Figure S6 and the initial gate leakage current can no longer be recovered as shown by the red line of Figure S6. This result means the insulating $In_2Se_{3-x}O_x$ is broken when the gate voltage exceeds 10 V.

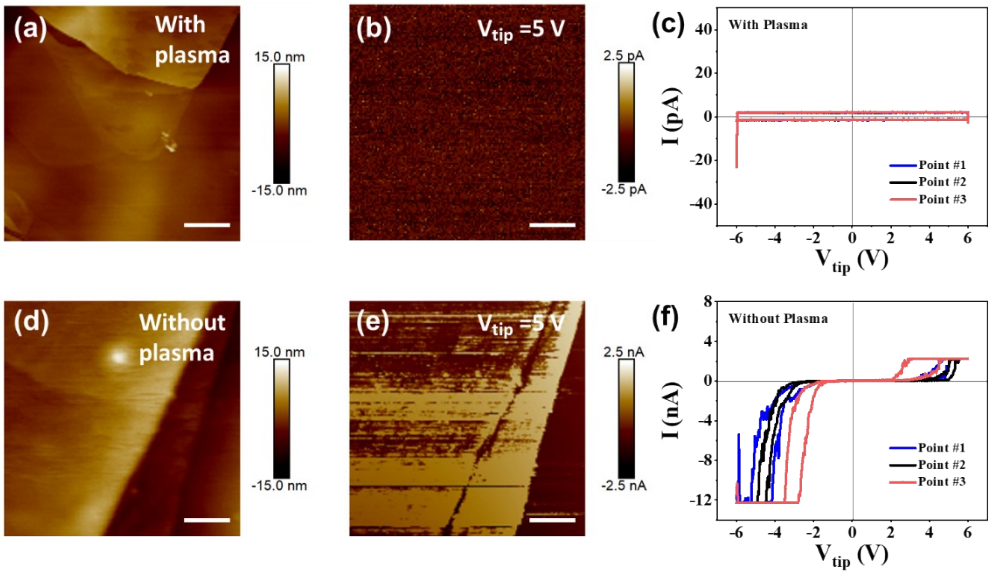

Figure S7. (a)-(c) The AFM images, conductive AFM mapping results and local I-V curves of In_2Se_3 device with oxygen plasma treatment. (d)-(f) The AFM image, conductive AFM mapping results and local I-V curves of In_2Se_3 device without oxygen plasma treatment. The scale bar is 600 nm.

When the voltage of the probe (V_{tip}) is 5V, the current of the In_2Se_3 device treated with oxygen plasma is below the noise level (pA) as shown in Figure S7(b). By contrast, the In_2Se_3 device without oxygen plasma treatment shows apparent currents of nA as shown in Figure S7(e). Subsequently, we performed localized I-V curves at three randomly selected points on the two samples as shown in S7(c)and (f), respectively. It is obvious that the insulator performance of the sample with oxygen plasma treatment is significantly better than that of the sample without oxygen plasma treatment. These results also indicate that the process of oxygen plasma treatment forms a high-quality insulating layer on the In_2Se_3 surface. Moreover, the hysteresis windows in the I-V curves are also agrees with the presence of ferroelectric properties in In_2Se_3 materials.

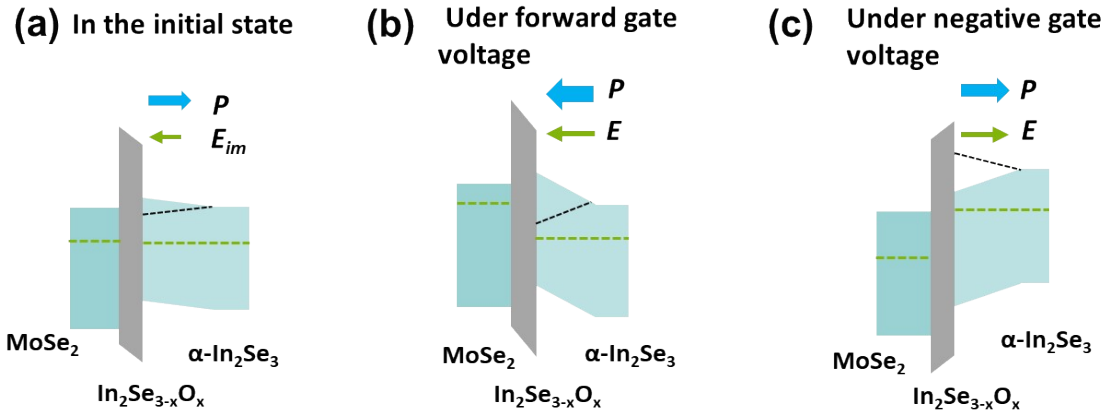

Figure S8. The expected schematic diagram of the band alignment of the design device (a) in the initial state, (b) under forward gate voltage and (c) under negative gate voltage.

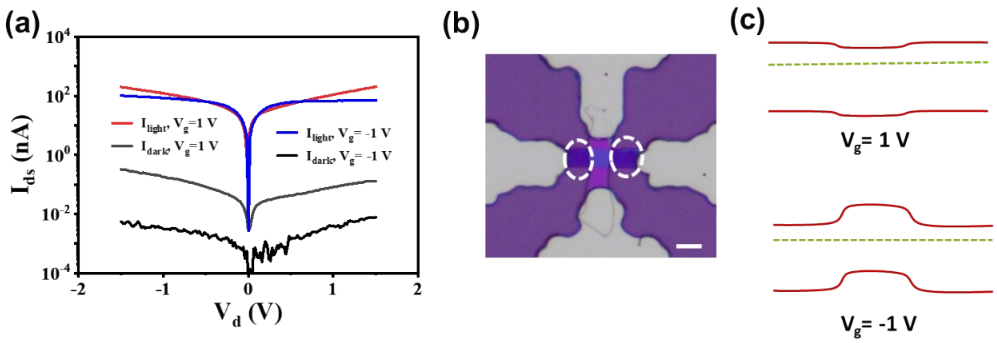

Figure S9. (a)The output curves in semi-log coordinates of the Fe-FET under illumination and in dark. (b) The optical microscopic image of the device. The scale bar is 5 μm. (c) The schematic diagram of the band alignment of the channel material.

The photocurrent at the negative gate voltage is less than that of the positive gate voltage when the Vds is greater than 1 V. This possible reason is that the ferroelectric gate does not regulate all the channel regions, as shown in Figure S9(b). At the negative gate voltage, the back-to-back PN junction prevents the dark current and the injected current at large bias, as shown in Figure S9(c).

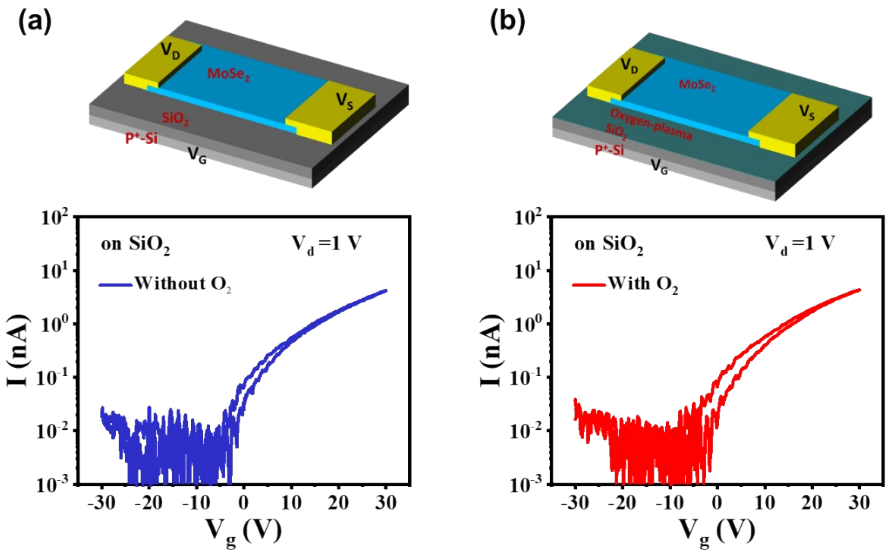

Figure S10. Schematic illustration and transfer curve of the FET device base on SiO_2 gate material (a) without oxygen-plasma treatment or (b) with oxygen-plasma treatment. The hysteresis window of these transfer curves did not change significantly after the oxygen-plasma treatment, indicating that the interface defect from the oxygen-plasma treatment did not obviously affect the hysteresis behavior of the transfer curve. Moreover, this tiny hysteresis window is very negligible compared to the ferroelectric gate devices.

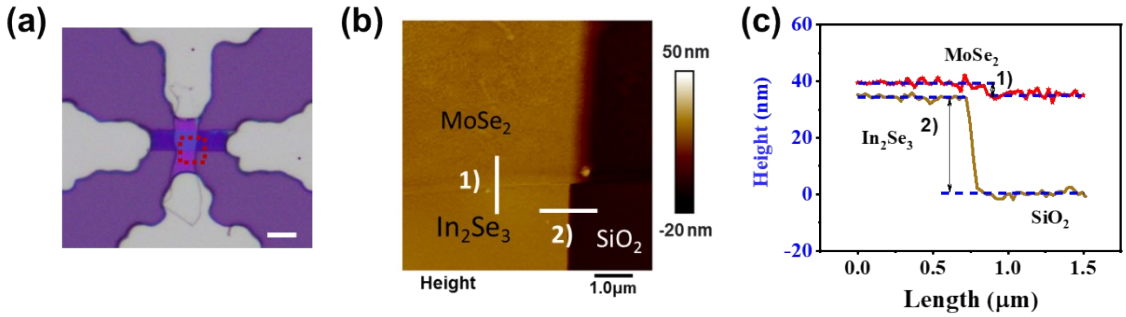

Figure S11. (a) The optical microscopic image of the Fe-FET. The scale bar is 5 μm. (b) The AFM maps for the red square in Figure S11(a). (c) The thickness profile along the white line positions of Figure S11(b), implying that the thicknesses of the $MoSe_2$ and α-In_2Se_3/$In_2Se_{3-x}O_x$ are about 6 nm, and 34 nm.

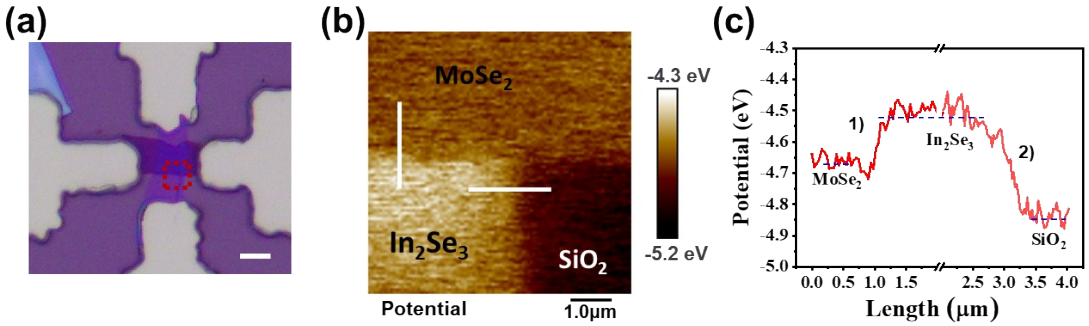

Figure S12. (a) The optical microscopic image of the device without oxygen plasma treatment, The scale bar is 5 μm. (b) The KPFM maps for the red sqare in Figure S12(a). (c) The relative Fermi potential of the $MoSe_2$ and α-In_2Se_3 from the white line in Figure S12(b).

the surface potential difference (be close to 180 mV) between $MoSe_2$ and In_2Se_3 without oxygen plasma treatment is greater than the potential difference (about 100 mV) between $MoSe_2$ and $In_2Se_{3-x}O_x$ with oxygen plasma treatment.

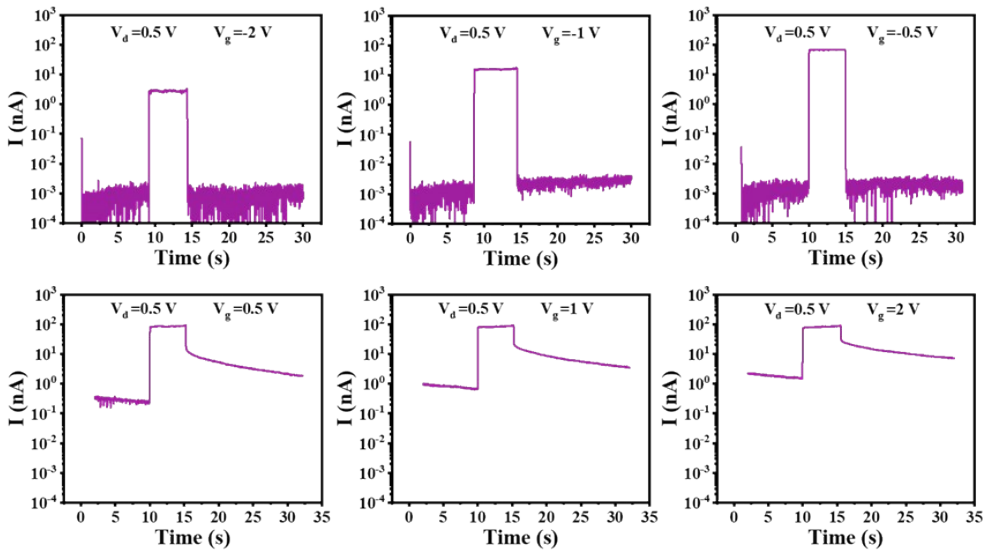

Figure S13. The time-resolved current under different gate voltages.

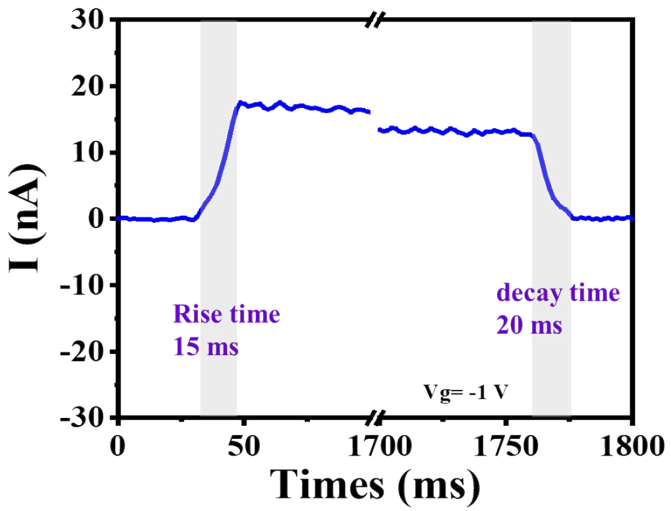

Figure S14. the photocurrent rapid change characteristics under -1 V gate voltage.

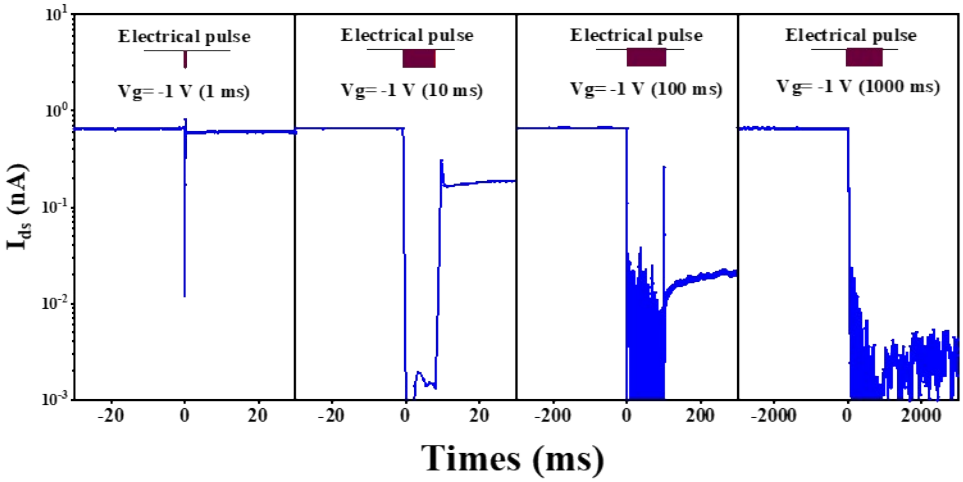

Figure S15. The forgetting behavior with different negative electric pulse widths. The estimation of electric energy consumption for the device is based on the following equations: $E_{electrical-erase} = V_g \times I_{gs} \times T_{pulse\ width}$.

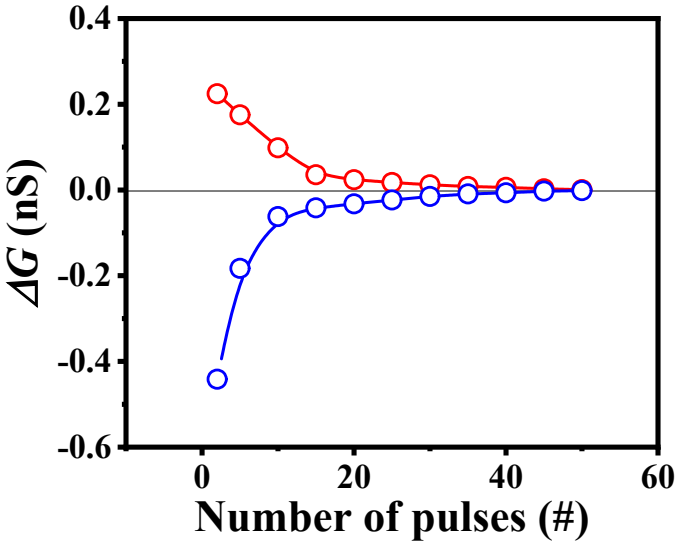

Figure S16. Change of conductance (*ΔG*) in the potentiation phase (application of optical spikes stimuli (red line)) and depression phase (application of electric spikes stimuli (blue line)).

Supplementary Note 2. Method to calculate C_{OX} and EOT.

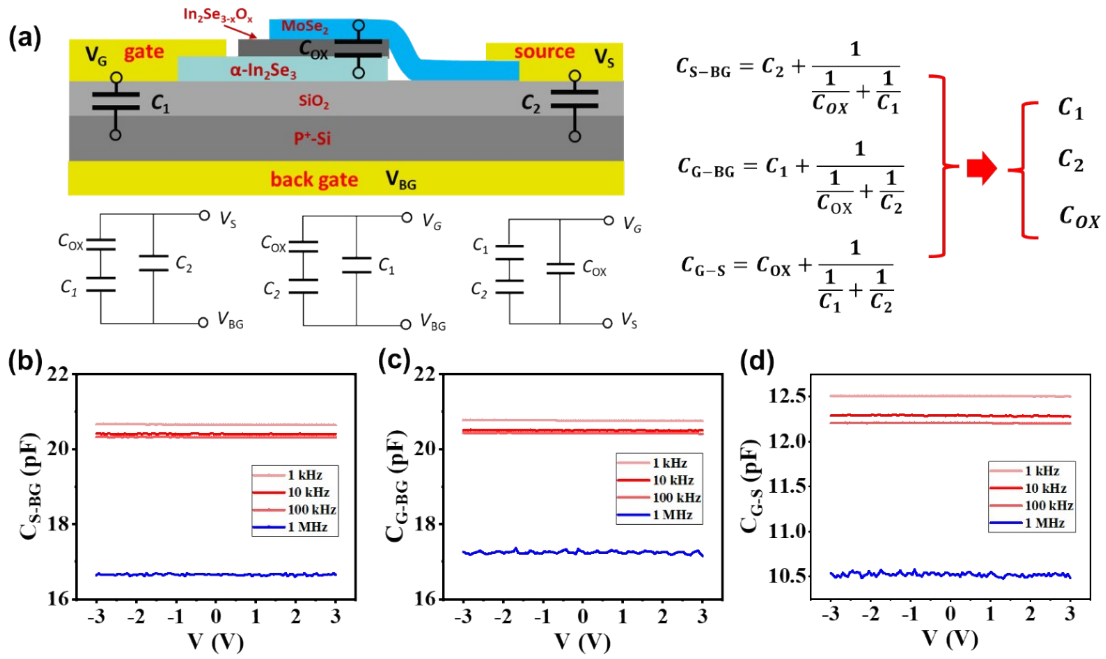

Figure S17. (a) The schematic diagram of the equivalent circuit during the capacitance test in the device. (b) The capacitance-voltage curves between the source and back gate (C_{S-BG}) under different frequencies. (c) The capacitance-voltage curves between the gate and back gate (C_{G-BG}) under different frequencies. (d) The capacitance-voltage curves between the gate and source (C_{G-S}) under different frequencies.

According to these equivalent circuits in Figure S17(a), we have the following equations,

$$C_{S-BG} = C_2 + \frac{1}{\frac{1}{C_{OX}} + \frac{1}{C_1}}$$

$$C_{G-BG} = C_1 + \frac{1}{\frac{1}{C_{OX}} + \frac{1}{C_2}} \quad (1)$$

$$C_{G-S} = C_{OX} + \frac{1}{\frac{1}{C_1} + \frac{1}{C_2}} \quad (2)$$

(3)

By solving the above system of equations, the values of C_{OX}, C_1 and C_2 are computed (for example, this value is calculated as 3.6 pF, 17.2 pF and 17.5 pF at 100 kHz, respectively). Statistical capacitance values from four devices are shown in Figure S18, which confirms the repeatability.

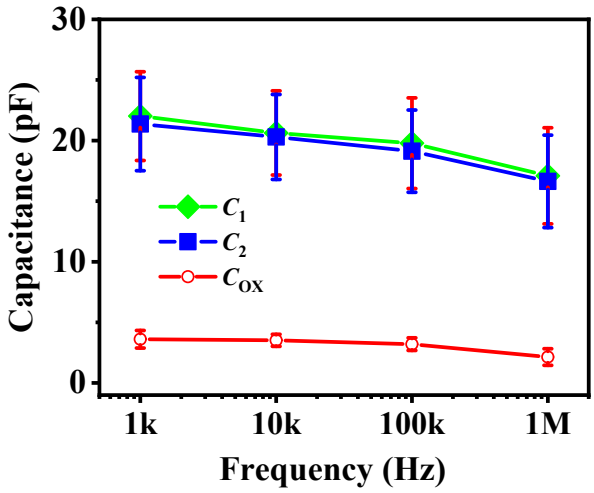

Figure S18. The statistical capacitance from four different devices.

Then, according to the capacitor calculation formula, namely

$$C = \frac{\varepsilon S}{4\pi k d} \quad (4)$$

the thicknesses of SiO_2 of the substrate and EOT of the $In_2Se_{3-x}O_x$ can be calculated. The thickness of SiO_2 is calculated to be about 280 nm at 1 kHz according to the calculated C_1 and C_2, which agrees with the practical SiO_2 thickness indicating that our test method is accurate. Using the same method, the EOT of the $In_2Se_{3-x}O_x$ is calculated to be about 0.15 nm to 0.2 nm according to the calculated C_{OX} as shown in Figure S19.

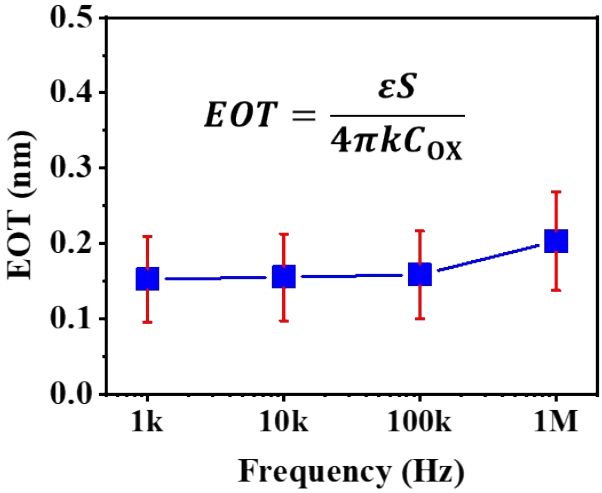

Figure S19. The values and computational formula of EOT at different frequencies.

Supplementary Note 3. The mechanism photoinduced change in polarization direction.

In accordance with Landau-Khalatnikov theory, the free energy in a system can be written as[3]

$$F = F_0 + \frac{\alpha}{2}\Psi^2 + \frac{\beta}{4}\Psi^4 + \ldots \quad (5)$$

Ψ is the order parameter. In a ferroelectric polarization system, the free energy is approximately expressed as[4]

$$F = F_0 + \frac{\alpha}{2}P^2 + \frac{\beta}{4}P^4 - EP \quad (6)$$

Here, the second-order coefficient of the polarization intensity *P* can be written as[3]

$$\alpha = \frac{2\pi}{C}(T - T_0) \quad (7)$$

T_0 is the phase transition temperature of the material (Curie temperature), C is the Curie-Weiss constant. For a stable system, the free energy should be in a minimum state. That is, the first order derivative is equal to 0 and the second order derivative is greater than 0 in Eq. 6.

In a ferroelectric polarization system, the system temperature is less than the Curie temperature, as shown in Figure RS20(a), the free energy appears two minimum with the different polarization intensity. This phenomenon indicate that the material system has two stable states and can be polarized. Generally, the polarization direction transition requires external energy assistance, as shown in the external electric field in Figure S20(b).

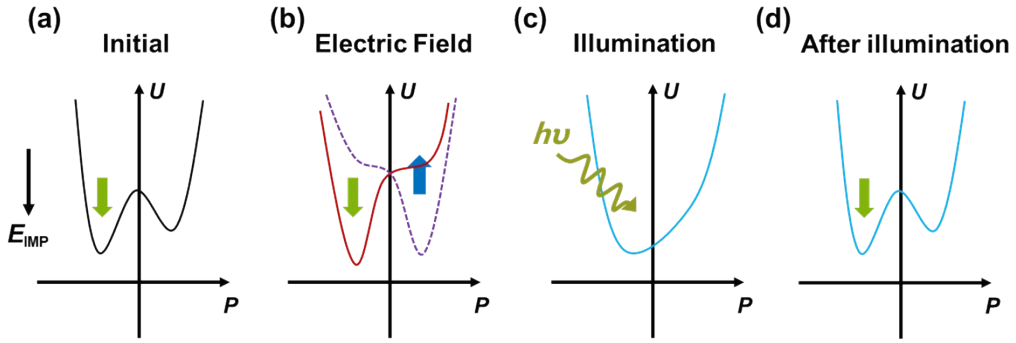

Figure S20. Schematic diagram of the relationship between system free energy and polarization intensity in photosensitive ferroelectric materials (a) the initial state in the presence of internal electric potential; (b) different reverse external electric field regulation; (c) during illumination; (d) after illumination.[5]

For a photosensitive ferroelectric material system, the carrier concentration is changed to *N* under illumination, the coefficient of each order in Eq. 6 needs to be updated, where the second order coefficient is updated to:[6]

$$\alpha \Rightarrow \alpha + aN \quad (8)$$

$$\beta \Rightarrow \beta + bN \quad (9)$$

The Curie temperature is also updated:

$$T_N - T_0 = -\frac{C}{2\pi}aN \quad (10)$$

T_N and T_0 are the Curie temperature at the electron concentration of *N* and 0, respectively. Therefore, the Curie temperature is altered under light-induced changes in carrier concentration in this photosensitive ferroelectric material system. This result changes the state of ferroelectric materials from the original polarized state to the non-polarized state. as shown in Figure S20(c). If there is a built-in potential in the photosensitive ferroelectric material system, no matter which is state the polarization direction before illumination? After illumination, the polarization direction will return to the state consistent with the built-in potential as shown in Figure S20(d).[7] That is, when the polarization state is different from the built-in potential before illumination, the polarization intensity of the device can be changed by illumination.

Supplementary Note 4. Dynamic switching characteristic under optical and electrical stimuli.

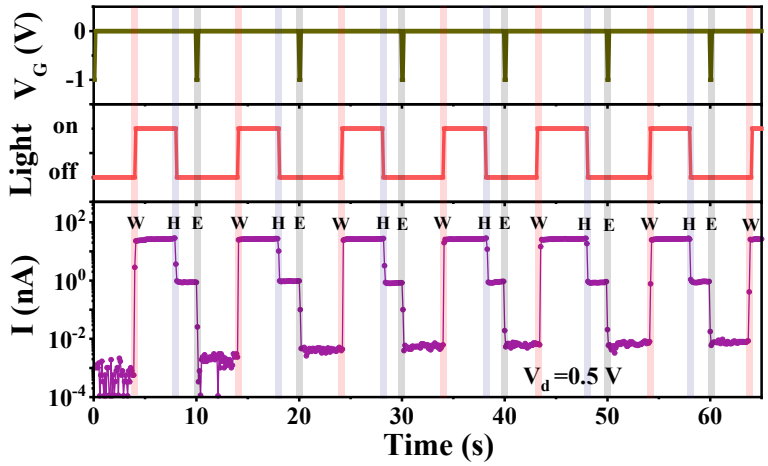

Figure S21. Dynamic switching characteristic of the photoelectric device under optical and electrical stimuli with a modulation cycle of optical-write and electrical-erase.

In the initial state, the device is firstly modulated to the off-state with a small dark current by a negative gate voltage pulse. Upon illumination, the output current immediately increases to the on-state as shown in point W of Figure S21 (optical-write process). After turning off the light, the device current is reduced to a residual value of about 1 nA as shown in point H of Figure S21 (hold on the memory state). Finally, a negative voltage pulse is needed to restore the current to the initial off-state as shown in point E of Figure S21 (electrical-erase process).

Table1. Performance parameters of the photodetector based on 2D ferroelectric material α-In_2Se_3.

2D Fe-FET material	on/off current ratio	Dark current (A)	Specific detectivity (Jones)	Response time	Reference
α-In_2Se_3	~10	10^{-10}	2.26×10^{12}	18 ms	[8]
α-In_2Se_3	2.9×10^{5}	1.2×10^{-13}	6.34×10^{17}	260 μs	[9]
α-In_2Se_3 /WSe_2	~10^4	10^{-10}	9.52×10^{10}	~3.3 ms	[10]
α-In_2Se_3 /WSe_2	2.56×10^{2}	1.4×10^{-10}	1.34×10^{11}	120 μs	[11]
α-In_2Se_3 /MoS_2	-	6.5×10^{-10}	6.2×10^{10}	20 ms	[12]
α-In_2Se_3 /Al_2O_3/MoS_2	10^5	10^{-11}	-	100 s	[13]
BP/α-In_2Se_3	4.82×10^{3}	2×10^{-11}	2.09×10^{12}	1260 μs	[14]
Gr/α-In_2Se_3/Gr	10^3	10^{-8}	4.4×10^{12}	-	[15]
$MoSe_2$/α-In_2Se_3	10^5	2×10^{-12}	1×10^{13}	20 ms	This work

Supplementary References

[1] Li, Y.; Chen, C.; Li, W.; Mao, X.; Liu, H.; Xiang, J.; Nie, A.; Liu, Z.; Zhu, W.; Zeng, H., Orthogonal electric control of the out-of-plane field-effect in 2D ferroelectric α-In_2Se_3. *Advanced Electronic Materials*, **2020**, *6* (7), 2000061.

[2] Giannazzo, F.; Fisichella, G.; Greco, G.; Di Franco, S.; Deretzis, I.; La Magna, A.; Bongiorno, C.; Nicotra, G.; Spinella, C.; Scopelliti, M., Ambipolar MoS_2 transistors by nanoscale tailoring of Schottky barrier using oxygen plasma functionalization. *ACS Applied Materials Interfaces*, **2017**, *9* (27), 23164-23174.

[3] Lo, V. C., Simulation of thickness effect in thin ferroelectric films using Landau–Khalatnikov theory. *Journal of Applied Physics*, **2003**, *94* (5), 3353-3359.

[4] Veng Cheong Lo; Chen, Z., Simulation of the Effects of Space Charge and Schottky Barriers on Ferroelectric Thin Film Capacitor Using Landau Khalatnikov Theory. *IEEE transactions on ultrasonics, ferroelectrics, and frequency control*, **2002**, *49* (7), 980-986.

[5] Long, X.; Tan, H.; Sanchez, F.; Fina, I.; Fontcuberta, J., Non-volatile optical switch of resistance in photoferroelectric tunnel junctions. *Nature Communications*, **2021**, *12* (1), 382.

[6] Íñiguez, J.; Zubko, P.; Luk'yanchuk, I.; Cano, A., Ferroelectric negative capacitance. *Nature Reviews Materials*, **2019**, *4* (4), 243-256.

[7] Xu, K.; Jiang, W.; Gao, X.; Zhao, Z.; Low, T.; Zhu, W., Optical control of ferroelectric switching and multifunctional devices based on van der Waals ferroelectric semiconductors. *Nanoscale*, **2020**, *12* (46), 23488-23496.

[8] Jacobs-Gedrim, R. B.; Shanmugam, M.; Jain, N.; Durcan, C. A.; Murphy, M. T.; Murray, T. M.; Matyi, R. J.; Moore, R. L.; Yu, B., Extraordinary photoresponse in two-dimensional In_2Se_3 nanosheets. *ACS Nano*, **2014**, *8* (1), 514-521.

[9] Yang, J.; Wang, F.; Guo, J.; Wang, Y.; Jiang, C.; Li, S.; Cai, Y.; Zhan, X.; Liu, X.; Cheng, Z.; He, J.; Wang, Z., Ultrasensitive ferroelectric semiconductor phototransistors for photon-level detection. *Advanced Functional Materials*, **2022**, *32* (36), 2205468.

[10] Jin, H. J.; Park, C.; Lee, K. J.; Shin, G. H.; Choi, S. Y., Ultrasensitive WSe_2/α-In_2Se_3 NIR photodetector based on ferroelectric gating effect. *Advanced Materials Technologies*, **2021**, *6* (11), 2100494.

[11] Zou, J.; Ke, Y.; Zhou, X.; Huang, Y.; Du, W.; Lin, L.; Wei, S.; Luo, L.; Liu, H.; Li, C.; Shen, K.; Ren, A.; Wu, J., Broadband visible-near Infrared two-dimensional WSe_2/In_2Se_3 photodetector for under water optical communications. *Advanced Optical Materials*, **2022**, *10* (12), 2200143.

[12] Cai, W.; Wang, J.; He, Y.; Liu, S.; Xiong, Q.; Liu, Z.; Zhang, Q., Strain-modulated photoelectric responses from a flexible α-In_2Se_3/3R MoS_2 Heterojunction. *Nano-micro Letters*, **2021**, *13* (1), 74.

[13] Parker, J.; Gu, Y., Highly efficient polarization-controlled electrical conductance modulation in a van der waals ferroelectric/semiconductor heterostructure. *Advanced Electronic Materials*, **2022**, *8* (9), 2200413.

[14] Zhu, C.; Wang, Y.; Wang, F.; Yang, J.; Zhan, X.; Fang, L.; Wang, Z.; He, J., Nonvolatile reconfigurable broadband photodiodes based on BP/α-In_2Se_3 ferroelectric p-n junctions. *Applied Physics Letters*, **2022**, *120* (8), 083101.

[15] Abderrahmane, A.; Woo, C.; Ko, P. J., Tunable optoelectronic properties of a two-dimensional graphene/α-In_2Se_3/graphene-based ferroelectric semiconductor field-effect transistor. *Journal of Materials Science: Materials in Electronics*, **2021**, *32* (15), 20252-20258.